

This article was downloaded by: [2008-2009 Thammasat University]

On: 9 February 2011

Access details: Access Details: [subscription number 789376256]

Publisher Taylor & Francis

Informa Ltd Registered in England and Wales Registered Number: 1072954 Registered office: Mortimer House, 37-41 Mortimer Street, London W1T 3JH, UK



## Drying Technology

Publication details, including instructions for authors and subscription information:

<http://www.informaworld.com/smpp/title~content=t713597247>

### One-Dimensional Model of Heat and Mass Transports and Pressure Built Up in Unsaturated Porous Materials Subjected to Microwave Energy

S. Sungsoontorn<sup>a</sup>; P. Rattanadecho<sup>a</sup>; W. Pakdee<sup>a</sup>

<sup>a</sup> Research Center of Microwave Utilization in Engineering (RCME), Department of Mechanical Engineering, Faculty of Engineering, Thammasat University (Rangsit Campus), Patumthani, Thailand

Online publication date: 19 January 2011

**To cite this Article** Sungsoontorn, S. , Rattanadecho, P. and Pakdee, W.(2011) 'One-Dimensional Model of Heat and Mass Transports and Pressure Built Up in Unsaturated Porous Materials Subjected to Microwave Energy', *Drying Technology*, 29: 2, 189 – 204

**To link to this Article:** DOI: 10.1080/07373937.2010.483029

**URL:** <http://dx.doi.org/10.1080/07373937.2010.483029>

PLEASE SCROLL DOWN FOR ARTICLE

Full terms and conditions of use: <http://www.informaworld.com/terms-and-conditions-of-access.pdf>

This article may be used for research, teaching and private study purposes. Any substantial or systematic reproduction, re-distribution, re-selling, loan or sub-licensing, systematic supply or distribution in any form to anyone is expressly forbidden.

The publisher does not give any warranty express or implied or make any representation that the contents will be complete or accurate or up to date. The accuracy of any instructions, formulae and drug doses should be independently verified with primary sources. The publisher shall not be liable for any loss, actions, claims, proceedings, demand or costs or damages whatsoever or howsoever caused arising directly or indirectly in connection with or arising out of the use of this material.

# One-Dimensional Model of Heat and Mass Transports and Pressure Built Up in Unsaturated Porous Materials Subjected to Microwave Energy

S. Sungsoontorn, P. Rattanadecho, and W. Pakdee

*Research Center of Microwave Utilization in Engineering (RCME),  
Department of Mechanical Engineering, Faculty of Engineering,  
Thammasat University (Rangsit Campus), Patumthani, Thailand*

In this article, the heat and mass transfer and pressure buildup in unsaturated porous media under microwave energy is theoretically investigated. The unsaturated porous media is composed of glass beads, water, and air. The microwave power generation is computed based on Lambert's law. The finite control volume (FCV) method is used to predict the heat and multiphase flow and pressure buildup in unsaturated porous media under various conditions. Most importantly, this work focuses on the influence of frequency, particle size, and electric field intensity to predict heat and mass transfer and pressure built up in porous media due to microwave energy. The results show that variations of frequency, particle size, and electric field intensity play an important role on overall drying kinetics. Furthermore, the findings of this research will serve as a fundamental tool for applications involving in the microwave drying process of porous media.

**Keywords** Electric field intensity; Frequency; Microwave energy; Particle size; Porous media; Pressure

## INTRODUCTION

Microwave is a form of electromagnetic wave, with wavelengths ranging from 1 m down to 1 mm, with frequencies between 0.3 and 300 GHz. Microwave is used in many industries and households as a source of thermal energy. It is used in the drying of textiles, paper, photographic film, and leather. Other uses include vulcanization, casting, and cross-linking polymers. Perhaps the largest consumption of microwave power is in the food industry, where it is used for cooking, thawing, freeze drying, sterilization, pasteurization, etc. Microwave energy can lower the drying temperature in several porous materials by several hundred degrees, shorten drying times, reduce drying defects, provide greater throughput, increase energy efficiency, and reduce floor-space requirements in comparison

with conventional drying methods. It is also environmentally friendly and integrates easily into flexible, automated manufacturing systems.

In order to maintain product quality, a uniform distribution of heat is of paramount importance in these processes. Factors that influence the uniform distribution of heat are load factors and microwave system factors. For example, dielectric properties, load geometry, and mixture ratio are load factors. Microwave system factors are turntable, operating frequency, placement inside the oven, oven size, and geometry. Knowledge of several parameters is required to accurately account for all the phenomena that occur in a dielectric heated by microwaves. This includes a description of the electromagnetic field distribution, microwave power absorption, temperature, and multiphase flow. For this reason, we need to solve the coupled differential equations including moisture transport equation, pressure equation, energy equation, and electromagnetic equation. Due to the complexity and number of equations involved, the numerical method is the only approach that conducts realistic process simulations.

A number of analyses of the drying process and the microwave heating process have appeared in recent research.<sup>[1–17]</sup> Excellent reviews of the drying techniques of porous material using microwave energy have been presented by Mujumdar,<sup>[18]</sup> Metaxas and Meridith,<sup>[19]</sup> Datta and Anantheswaran,<sup>[20]</sup> and Schubert and Regier.<sup>[21]</sup> Recently, Perré and May<sup>[22]</sup> systematically presented multiple sets of macroscopic equations proposed for simulation of the drying process. Considerations concerning the potential of these formulations, together with the number of space dimensions used in the simulation, were discussed in detail. The first fundamental difference between them lies in the number of state variables used to describe the medium:

1. Model 1, three variables: moisture content (or an equivalent variable: saturation, water potential), temperature (or an equivalent variable: enthalpy), and

Correspondence: P. Rattanadecho, Research Center of Microwave Utilization in Engineering (RCME), Department of Mechanical Engineering, Faculty of Engineering, Thammasat University (Rangsit Campus), 99 Moo 18, Patumthani 12120, Thailand; E-mail: ratphadu@engr.tu.ac.th

gaseous pressure (or an equivalent variable: air density, intrinsic air density).

2. Model 2, two variables: moisture content (or equivalent variable) and temperature (or an equivalent variable).
3. Model 3, one variable: moisture content (or equivalent variable).

Although a number of studies were conducted to investigate the microwave heating and drying processes, most were carried out using a simplified model, that is, model 2 or model 3, as defined above. A few papers focused on model 1.<sup>[22]</sup> Furthermore, in previous work, the influences of the frequency, particle size, and electric field intensity on the drying kinetics have not been clearly studied. In general, during the microwave drying process of porous material, the phenomenon is too complex for theoretical explanation, due to the strong effects of the interaction between dielectric material and wave characteristics. Consequently, from a macroscopic point of view, these effects on heat and mass transport and microwave-absorbed energy within porous material during the microwave drying process must be clarified in detail. This current study is extended from the work of Ratanadecho et al.<sup>[10]</sup> to systematically investigate the influences of frequency, particle size, and electric field intensity on the overall drying kinetics. In the present study, the model formulation is based on model 1, as defined earlier. The comprehensive set of equations used at macroscopic level describes the system using three independent state variables. A more detailed description of these equations and related assumptions can be found in the relevant section. In analysis of the microwave energy absorbed term, the energy absorption is assumed to decay exponentially into the sample following Lambert's law. Most importantly, this study focuses on the results of the distributions of microwave-absorbed energy, temperature, and moisture profiles within the porous materials. Furthermore, the multiphase flow behavior is discussed in detail. The results presented herein provide a basis for fundamental understanding of the microwave drying of porous materials.

**RELATED THEORIES**

Figure 1 shows the analytical model for microwave drying of the sample. The rate of volumetric energy absorbed corresponding to the microwave-absorbed energy was assumed to decay exponentially into the sample, according to Lambert's law. The basic equation to calculate the density of microwave power absorbed by dielectric material can be written in the final form as<sup>[10]</sup>:

$$Q = -\frac{\partial P}{\partial z} dz = 2\alpha P dz = 2\alpha dz \cdot 2\pi f \epsilon(\tan \delta) E^2 e^{-2\alpha z} \quad (1)$$

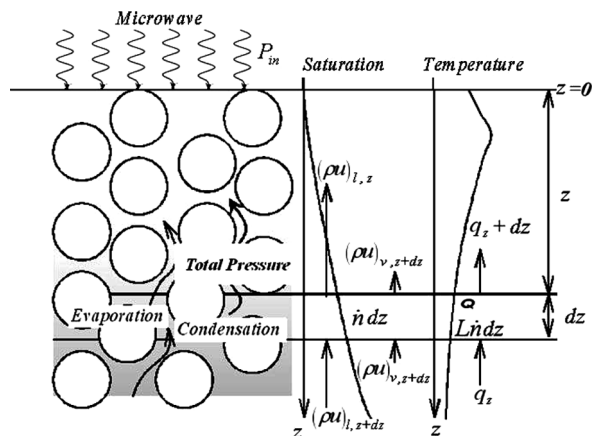


FIG. 1. Analytical model.

where  $E$  is the electromagnetic field intensity;  $f$  is the frequency of the microwave;  $\omega$  is the angular velocity of the microwave;  $\tan \delta$  is the dielectric loss tangent coefficient; and  $\alpha$  is the attenuation constant, which can be calculated from<sup>[10]</sup>:

$$\begin{aligned} \alpha &= 2\pi f \sqrt{\frac{\epsilon_0 \epsilon_r \mu_0}{2}} (\sqrt{\tan^2 \delta + 1} - 1) \\ &= \frac{2\pi f}{c} \sqrt{\frac{\epsilon_r}{2}} (\sqrt{\tan^2 \delta + 1} - 1) \end{aligned} \quad (2)$$

The attenuation parameter ( $\alpha$ ) controls the rate at which the incident field decays and is inversely proportional to the skin depth; that is,  $\alpha = 1/\delta_s$ . In this work, the effects of the overall drying kinetics are examined by selecting the dielectric properties as a function of water saturation (moisture content) and temperature. The theory mixing the formulas by Wang and Schmutge<sup>[23]</sup> is used.

The loss tangent coefficient can be expressed as follows:

$$\tan \delta = \frac{\epsilon''}{\epsilon'} \quad (3)$$

where  $\epsilon''$  is a dielectric loss factor and  $\epsilon'$  is a dielectric constant.

The dielectric properties of water taken from Von Hippel<sup>[24]</sup> are a function of temperature. The dielectric properties of gas are assumed constant. The numerical values for skin depth, relative permittivity, and loss tangent at various moisture contents are listed in Table 1.

The main transport mechanisms that enable moisture movement during the microwave drying of the sample are liquid flows driven by capillary pressure gradient and gravity. However, the vapor is driven by the gradient of the partial pressure of the evaporating species. The main

TABLE 1  
Dielectric properties of the sample (corresponding to  
 $T = 20^\circ\text{C}$  and  $f = 2.45\text{ GHz}$ )<sup>[10]</sup>

Moisture content (s)	Relative permittivity ( $\epsilon_r'$ )	Loss tangent ( $\tan \delta$ )	Skin depth ( $\delta_s$ )
0.0	3.5420	0.0062	3.338119
0.25	10.9606	0.0190	0.607039
0.5	18.3110	0.0319	0.285429
0.75	25.6955	0.0447	0.171784
1.0	33.0801	0.0589	0.117645

assumptions involved in the formulation of the transport model are the following:

1. The capillary porous material is rigid. No chemical reactions occur in the sample.
2. The local thermodynamics equilibrium among phases is assumed.
3. The gas phase is ideal in the thermodynamic sense.
4. The contribution of convection to energy transport is included.
5. Darcy's law holds valid for the liquid and gas phases.
6. Gravity is included, particularly in the liquid and gas phases.
7. The permeability of liquid and gas can be expressed in terms of relative permeability.
8. In a macroscopic sense, the packed bed is assumed to be homogeneous and isotropic, and liquid water is not bound to the solid matrix. Therefore, the volume average model for a homogeneous and isotropic material can be used in the theoretical model and analysis.
9. Corresponding to the electric field, the temperature and moisture profiles are assumed to have a one-dimensional form.
10. The microwave absorbed energy is assumed to decay exponentially into the sample, according to Lambert's law.
11. The nonthermal effect of microwave irradiation is neglected.

### Mass Conservation

The macroscopic mass conservation equations for liquid, water vapor, air, and gas phases are written, respectively, as:

$$\text{Liquid phase: } \rho_l \phi \frac{\partial s}{\partial t} + \rho_l \frac{\partial u_l}{\partial z} = -\dot{n} \quad (4)$$

$$\text{Vapor phase: } \frac{\partial}{\partial t} (\rho_v \phi (1-s)) + \frac{\partial}{\partial z} (\rho_v u_v) = \dot{n} \quad (5)$$

$$\text{Air phase: } \frac{\partial}{\partial t} (\rho_a \phi (1-s)) + \frac{\partial}{\partial z} (\rho_a u_a) = 0 \quad (6)$$

$$\text{Gas phase: } \frac{\partial}{\partial t} (\rho_g \phi (1-s)) + \frac{\partial}{\partial z} (\rho_g u_g) = \dot{n} \quad (7)$$

where  $\dot{n}$  is the condensation rate or the evaporation rate during a phase change. The water vapor and air mass flux are the sum of the convective term with the gas superficial velocity and diffusive term.

### Energy Conservation

The temperature of the sample exposed to irradiation is obtained by solving the conventional heat transport equation with the microwave energy absorbed included as a local heat generation term. The governing energy equation describing the temperature rise in the sample is the time. The energy conservation equation is represented by:

$$\begin{aligned} \frac{\partial}{\partial t} ((\rho C_p)_T T) + \frac{\partial}{\partial z} ((\rho_l C_{pl} u_l + (\rho_a C_{pa} + \rho_v C_{pv}) u_g) T) \\ + H_v \dot{n} = \frac{\partial}{\partial z} \left( \lambda \frac{\partial T}{\partial z} \right) + Q \end{aligned} \quad (8)$$

### Phenomenological Relations

In order to complete the system of equations, the expressions for the superficial average velocity of the liquid and gas phases, the generalized Darcy's law in the following form was used by Ratanadecho et al.<sup>[10]</sup>:

$$u_l = -\frac{KK_{rl}}{\mu_l} \left[ \frac{\partial P_g}{\partial z} - \frac{\partial P_c}{\partial z} - \rho_l g \right], u_g = -\frac{KK_{rg}}{\mu_g} \left[ \frac{\partial P_g}{\partial z} - \rho_g g \right] \quad (9)$$

where  $\mu_l$  and  $\mu_g$  denote the viscosity of liquid and gas phases, respectively.

For the velocity of water vapor and air phases, the generalized Fick's law in the following form is used:

$$\rho_v u_v = \rho_v u_g - \rho_g D_m \frac{\partial}{\partial z} \left( \frac{\rho_v}{\rho_g} \right), \rho_a u_a = \rho_a u_g - \rho_g D_m \frac{\partial}{\partial z} \left( \frac{\rho_a}{\rho_g} \right) \quad (10)$$

where the capillary pressure ( $P_c$ ) is related to the gas and liquid phases and can be written as:

$$P_c = P_g - P_l \quad (11)$$

and  $D_m$  is the effective molecular mass diffusion<sup>[10]</sup>:

$$D_m = \frac{2\phi}{3-\phi} (1-s)D \quad (12)$$

### Equilibrium Relations

The system of conservation equations obtained for multiphase transport mode requires a constitutive equation for liquid relative permeability  $K_{rl}$  and gas relative permeability  $K_{rg}$ . A typical set of constitutive relationships for liquid and gas system was given by Ratanadecho et al.<sup>[10]</sup>:

$$K_{rl} = s_e^3, K_{rg} = 1.2984 - 1.9832s_e + 0.7432s_e^2 \quad (13)$$

where  $s_e$  is the effective water saturation considering the irreducible water saturation ( $s_{ir} = 0.06$ ) and is defined by:

$$s_e = \frac{s - s_{ir}}{1 - s_{ir}} \quad (14)$$

The capillary pressure is further assumed to be adequately represented by Leverett's well-known  $J(s_e)$  functions, and the relationship between the capillary pressure and the water saturation is defined by using Leverett functions  $J(s_e)$ :

$$P_c = P_g - P_l = \frac{\sigma}{\sqrt{K/\phi}} J(s_e) \quad (15)$$

Here  $\sigma$  is the gas-liquid interfacial tension, and Leverett functions are given by:

$$J(s_e) = 0.325(1/s_e - 1)^{0.217} \quad (16)$$

Figure 2 shows the typical moisture characteristic curve (the relationship between capillary pressure and water saturation) for different particle sizes obtained from present experiments. It can be seen that, in the case of the same water saturation, a small particle size corresponds to a higher capillary pressure. The characteristics of water transport in porous material obtained here are shown in Table 2.

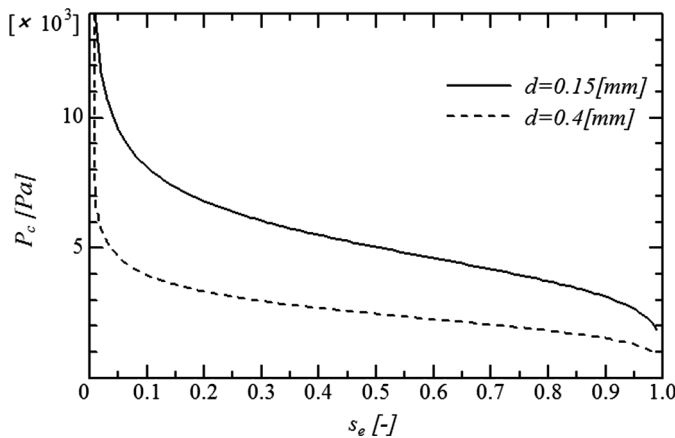


FIG. 2. Typical relationship between  $P_c$  and  $s_e$ .<sup>[10]</sup>

TABLE 2

Characteristics of water transport in porous material<sup>[10]</sup>

Diameter, $d$ (mm)	Porosity, $\phi$	Permeability, $k$ (m <sup>2</sup> )
0.15	0.385	$8.41 \times 10^{-12}$
0.4	0.371	$3.52 \times 10^{-11}$

The effective thermal conductivity of the capillary porous medium is a function of water saturation that can be written as:

$$\lambda = \frac{0.8}{1 + 3.78e^{-5.95s}} \quad (17)$$

### Stated Equations

The gas phase is assumed to be an ideal mixture of air and vapor, so the density of each phase can be determined by the stated equations,<sup>[15]</sup>

$$\rho_a = \frac{P_a M_a}{R_o T}$$

$$\rho_v = \frac{P_v M_v}{R_o T}$$

$$\rho_g = \rho_a + \rho_v$$

$$P_a = \rho_a R_a T$$

$$P_v = \rho_v R_v T$$

$$\rho_g u_g = \rho_a u_g + \rho_v u_v \quad (18)$$

The partial pressure of the vapor is given by Kelvin's equation, based on the capillary force as defined by:

$$P_v = P_{vs} \exp\left(\frac{P_c}{\rho_l R_v T}\right) \quad (19)$$

where  $P_{vs}$  is the partial pressure of the saturation vapor.

### Heat Transport Equation

The kinetic energy and pressure terms, which are usually unimportant, are ignored. Local thermodynamics equilibrium among all phases is assumed. The temperature of unsaturated porous media is obtained by solving the conventional heat transport equation. Considering the enthalpy transport based on the water and gas flows,

the conduction heat and latent heat transfer are due to evaporation. The energy conservation equation is represented by:

$$\begin{aligned} & \frac{\partial}{\partial t}((\rho C_p)_T T) + \frac{\partial}{\partial z}((\rho_l C_{pl} w_l + (\rho_a C_{pa} + \rho_v C_{pv}) w_g) T) \\ &= \frac{\partial}{\partial z} \left( \lambda \frac{\partial T}{\partial z} \right) - H_v \left( \frac{\partial}{\partial t} (\rho_v \phi (1-s)) \right. \\ & \left. + \frac{\partial}{\partial z} \left( \rho_v \frac{KK_{rg}}{\mu_g} \left( -\frac{\partial P_g}{\partial z} + \rho_g g_z \right) - \rho_g D_m \frac{\partial}{\partial z} \left( \frac{\rho_v}{\rho_g} \right) \right) \right) + Q \end{aligned} \quad (20)$$

### Mass Transport Equation

The phenomenon of moisture transport is described by the mass conservation equations for the liquid phase and for the water vapor in the gas phase because the total water content is of interest. The addition of the one-dimensional equations (Eqs. (4) and (5)) yields total moisture content as follows:

$$\begin{aligned} & \phi \frac{\partial}{\partial t} \{s + Y_v(1-s)\} + \frac{\partial}{\partial z} \left[ \frac{KK_{rl}}{\mu_l} \left( \frac{\partial P_c}{\partial z} - \frac{\partial P_g}{\partial z} + g_z \right) \right. \\ & \left. + Y_v \frac{KK_{rg}}{\mu_g} \left( -\frac{\partial P_g}{\partial z} + \rho_g g_z \right) - Y_g D_m \frac{\partial}{\partial z} (W_v) \right] = 0 \end{aligned} \quad (21)$$

where  $\frac{\rho_v}{\rho_l} = Y_v$ ,  $\frac{\rho_g}{\rho_l} = Y_g$ ,  $\frac{\rho_a}{\rho_l} = Y_a$ , and  $\frac{Y_v}{Y_g} = W_v$

### The Pressure Built Up in Porous Media Equation

The pressure built up in the porous media is obtained from the air-balance equation (Eq. (6)) as follows:

$$\begin{aligned} & \phi \frac{\partial}{\partial t} \{Y_a(1-s)\} + \frac{\partial}{\partial z} \left[ Y_a \frac{KK_{rg}}{\mu_g} \left( -\frac{\partial P_g}{\partial z} + \rho_g g_z \right) \right. \\ & \left. - Y_g D_m \frac{\partial}{\partial z} \left( \frac{\rho_a}{\rho_g} \right) \right] = 0 \end{aligned} \quad (22)$$

### Boundary and Initial Conditions

The boundary conditions proposed for the open boundary of the sample define the exchange of energy at the open boundary, which can be described in the following form:

$$-\lambda \frac{\partial T}{\partial z} = h_c (T - T_a) \quad (23)$$

$$\rho_l w_l + \rho_v w_v = h_m (\rho_v - \rho_{va}) \quad (24)$$

where  $h_c$  is the heat transfer coefficient,  $h_m$  is the mass transfer coefficient,  $\rho_v$  is the density of water vapor at the open boundary, and  $\rho_{va}$  is reference vapor density in the gas phase surrounding the open boundary. The boundary conditions at the symmetrical impermeable surface are given by:

$$\frac{\partial T}{\partial z} = 0, \quad \frac{\partial w}{\partial z} = 0 \quad (25)$$

### NUMERICAL PROCEDURE

The system of nonlinear partial differential equations (Eqs. (20)–(25)) must be solved by the finite difference method based on the notation of control volume as described by Patankar.<sup>[25]</sup> At each time increment, the nodal values of  $s$ ,  $T$ , and  $P$  were solved iteratively and convergence was checked on both variables. The Newton-Raphson method was employed at each iteration to speed up the convergence. The discretized form of the heat transport equation (Eq. (20)) is given by:

$$\begin{aligned} & \frac{(\rho C_p)_{Tk}^{n+1} T_k^{n+1} - (\rho C_p)_{Tk}^n T_k^n}{\Delta t} + \frac{\rho_l C_{pl}}{\Delta z} (w_{lk}^{n+1} T_k^{n+1} - w_{lk-1}^{n+1} T_{k-1}^{n+1}) + \frac{(\rho C_p)_{av}}{\Delta z} (w_{gk}^{n+1} T_k^{n+1} - w_{gk-1}^{n+1} T_{k-1}^{n+1}) \\ & - \frac{1}{\Delta z} \left( \lambda_{k+\frac{1}{2}}^{n+1} \left( \frac{T_{k+1}^{n+1} - T_k^{n+1}}{\Delta z} \right) - \lambda_{k-\frac{1}{2}}^{n+1} \left( \frac{T_k^{n+1} - T_{k-1}^{n+1}}{\Delta z} \right) \right) + \frac{H_v \rho_v \phi}{\Delta t} ((1-s_{ir})(s_{ek}^{n+1} - s_{ek}^n)) \\ & - \frac{1}{\Delta z} \left( \left( \rho_{vk} \frac{KK_{rg}}{\mu_g} \Big|_{k+\frac{1}{2}} \left( -\left( \frac{P_{gk+1}^{n+1} - P_{gk}^{n+1}}{\Delta z} \right) + \rho_g g_z \right) - \rho_{vk-1} \frac{KK_{rg}}{\mu_g} \Big|_{k-\frac{1}{2}} \left( -\left( \frac{P_{gk}^{n+1} - P_{gk-1}^{n+1}}{\Delta z} \right) + \rho_g g_z \right) \right) \right) \\ & - \frac{1}{\Delta z} \left( -\left( \rho_{gk} D_{mk+\frac{1}{2}}^{n+1} \left( \frac{\left( \frac{\rho_v}{\rho_g} \right)_{k+1}^{n+1} - \left( \frac{\rho_v}{\rho_g} \right)_k^{n+1}}{\Delta z} \right) - \rho_{gk-1} D_{mk-\frac{1}{2}}^{n+1} \left( \frac{\left( \frac{\rho_v}{\rho_g} \right)_k^{n+1} - \left( \frac{\rho_v}{\rho_g} \right)_{k-1}^{n+1}}{\Delta z} \right) \right) \right) - Q = 0 \end{aligned} \quad (26)$$

Similarly, the discretized form of the mass transport equation (Eq. (21)) can be written as

$$\frac{\phi}{\Delta t} (1 - s_{ir}) ((s_{ek}^{n+1} - s_{ek}^n) + (Y_{vk}^{n+1}(1 - s_{ek}^{n+1}) - Y_{vk}^n(1 - s_{ek}^n))) + \frac{1}{\Delta z} \left( \left( \frac{KK_{rl}}{\mu_l} \Big|_{k+\frac{1}{2}} \left( \left( \frac{P_{ck+1}^{n+1} - P_{ck}^{n+1}}{\Delta z} \right) - \left( \frac{P_{gk+1}^{n+1} - P_{gk}^{n+1}}{\Delta z} \right) + g_z \right) - \frac{KK_{rl}}{\mu_l} \Big|_{k-\frac{1}{2}} \left( \left( \frac{P_{ck}^{n+1} - P_{ck-1}^{n+1}}{\Delta z} \right) - \left( \frac{P_{gk}^{n+1} - P_{gk-1}^{n+1}}{\Delta z} \right) + g_z \right) \right) + Y_{vk}^{n+1} \left( \frac{KK_{rg}}{\mu_g} \Big|_{k+\frac{1}{2}} \left( - \left( \frac{P_{gk+1}^{n+1} - P_{gk}^{n+1}}{\Delta z} \right) + \rho_g g_z \right) - \frac{KK_{rg}}{\mu_g} \Big|_{k-\frac{1}{2}} \left( - \left( \frac{P_{gk}^{n+1} - P_{gk-1}^{n+1}}{\Delta z} \right) + \rho_g g_z \right) \right) - Y_{gk}^{n+1} \left( D_{mk+\frac{1}{2}}^{n+1} \left( \frac{W_{vk+1}^{n+1} - W_{vk}^{n+1}}{\Delta z} \right) - D_{mk-\frac{1}{2}}^{n+1} \left( \frac{W_{vk}^{n+1} - W_{vk-1}^{n+1}}{\Delta z} \right) \right) \right) = 0 \quad (27)$$

The discretized form of the pressure built up in the porous media equation (Eq. (22)) can also be written as:

$$\frac{\phi}{\Delta t} ((1 - s_{ir})(Y_{ak}^{n+1}(1 - s_{ek}^{n+1}) - Y_{ak}^n(1 - s_{ek}^n))) + \frac{1}{\Delta z} \left( Y_{ak}^{n+1} \left( \frac{KK_{rg}}{\mu_g} \Big|_{k+\frac{1}{2}} \left( - \left( \frac{P_{gk+1}^{n+1} - P_{gk}^{n+1}}{\Delta z} \right) + \rho_g g_z \right) - \frac{KK_{rg}}{\mu_g} \Big|_{k-\frac{1}{2}} \left( - \left( \frac{P_{gk}^{n+1} - P_{gk-1}^{n+1}}{\Delta z} \right) + \rho_g g_z \right) \right) - Y_{gk}^{n+1} \left( D_{mk+\frac{1}{2}}^{n+1} \left( \frac{\left( \frac{\rho_a}{\rho_g} \right)_{k+1}^{n+1} - \left( \frac{\rho_a}{\rho_g} \right)_k^{n+1}}{\Delta z} \right) - D_{mk-\frac{1}{2}}^{n+1} \left( \frac{\left( \frac{\rho_a}{\rho_g} \right)_k^{n+1} - \left( \frac{\rho_a}{\rho_g} \right)_{k-1}^{n+1}}{\Delta z} \right) \right) \right) = 0 \quad (28)$$

2.45 and 5 GHz. However, there are other fixed parameters including the particle size of 0.15 mm, the electric field

intensity of 4,200 V/m, and the initial moisture content of 0.7. The microwave energy absorbed is shown in Fig. 5.

Details of the computational schemes and strategy are illustrated in Fig. 3. The electromagnetic and thermophysical properties used in the computation are given in Table 3. To verify the accuracy of the presented numerical study, the resulting data are validated against the results obtained by Kaviany and Rogers.<sup>[26]</sup> Figure 4a shows the predicted result<sup>[26]</sup> and Fig. 4b shows the results from the present study. Both are in good agreement. At  $t = 114$  min, the study shows that the distribution curve gradually declines at unheated surface from  $X/L$  of 0.7 onwards. This suggests that the additional conditions in the present model under the same numerical approach yield a nontrivial difference at  $t = 114$  min.

**RESULTS AND DISCUSSION**

In this section, the effects of various parameters on microwave drying are investigated. The effects of microwave frequency ( $f$ ) are examined first, followed by the effects of particle size and electric field intensity.

**Influence of Frequency**

The case of frequency effects is the first condition. The numerical results are based on two different frequencies,

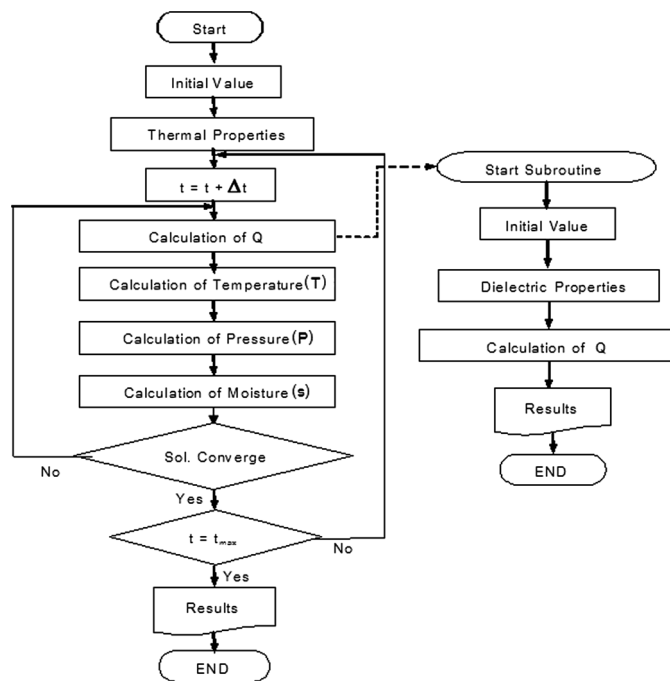
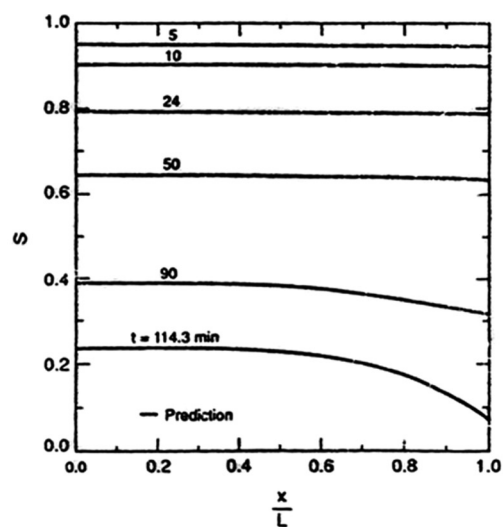


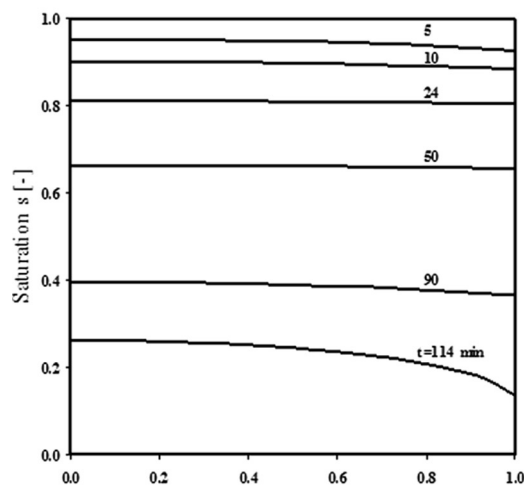
FIG. 3. Computational scheme.

TABLE 3  
Electromagnetic and thermophysical properties used in the computations

$\epsilon_0 = 8.85419 \times 10^{12} [F/m]$	$\epsilon_{ra} = 1.0$	$\epsilon_{rp} = 5.1$
$\mu_0 = 4.0\pi \times 10^{-7} [H/m]$	$\mu_{ra} = 1.0$	$\mu_{rp} = 1.0$
$\mu_{rl} = 1.0$	$\tan \delta_a = 0.0$	$\tan \delta_p = 0.01$
$\rho_a = 1.205 [kg/m^3]$	$\rho_p = 2,500 [kg/m^3]$	$\rho_l = 1,000 [kg/m^3]$
$C_{pa} = 1.007 [kJ/(kg \cdot K)]$	$C_{pp} = 0.80 [kJ/(kg \cdot K)]$	$C_{pl} = 4.186 [kJ/(kg \cdot K)]$
$\lambda_a [W/(m \cdot K)]$	$\lambda_p = 1.0 [W/(m \cdot K)]$	$\lambda_l = 0.610 [W/(m \cdot K)]$
Initial saturation ( $s$ ) = 0.7	$T_{air} = 30^\circ C$	
$htc = 15 [W/(m^2 \cdot K)]$	$hr = 0.58 [m/s]$	



(a)



(b)

FIG. 4. Saturation profiles with respect to elapsed time: (a) result predicted<sup>[26]</sup> and (b) result predicted from present study.

In Fig. 5, it can be seen that the maximum value of the microwave energy absorbed occurs at a depth of 2 cm and decreases with increasing elapsed time. Therefore, continued drying would eventually cause the average moisture content inside the sample to decrease and lead to a decrease in microwave energy absorbed. This phenomenon explains why the microwave energy absorbed within the sample in the end stage of drying (10 h) is slightly lower than that observed in the early stage of drying. This result is the same in the case of higher frequency. In Fig. 6, it is seen that the temperature profile within the sample rises quickly in the early stage of the drying process, after which it slows down considerably, because the dielectric loss coefficient decreases significantly with increasing temperature. This is the same reason that the microwave energy absorbed in the last stage of drying is lower as shown in Fig. 5. Distributions of temperature have trends similar to the distributions of energy absorbed depicted in Fig. 5.

Figure 7 shows the moisture profiles for two frequencies ( $f = 2.45$  GHz and  $f = 5$  GHz) that correspond to the initial moisture content of 0.7. The observed moisture profiles in the case of higher frequency are lower than those in the

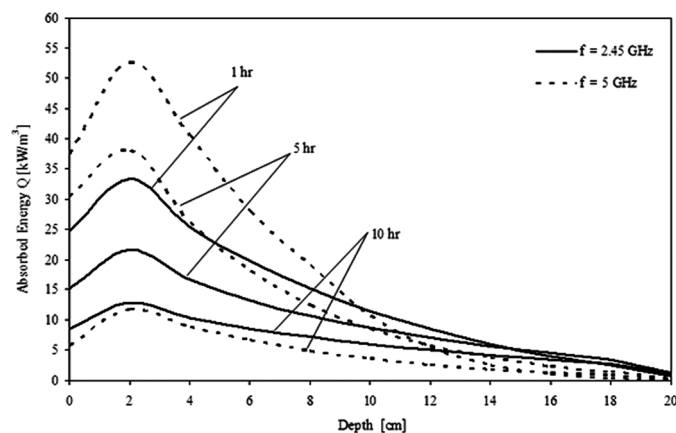


FIG. 5. Energy absorbed profiles at various frequencies ( $d = 0.15$  mm,  $E_{in} = 4,200$  V/m,  $S_{in} = 0.7$ ).

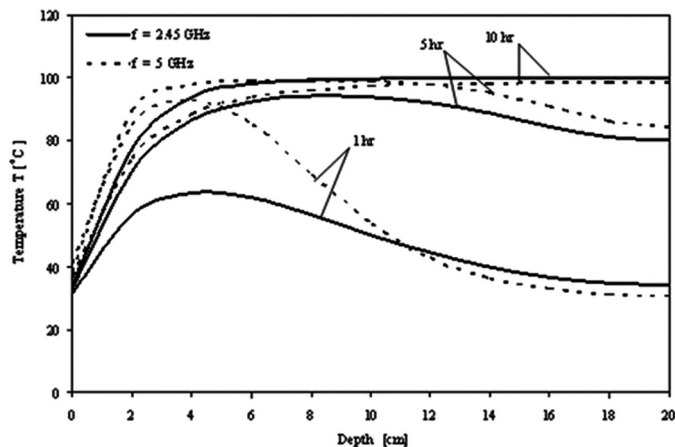


FIG. 6. Temperature profiles at various frequencies ( $d=0.15$  mm,  $E_{in}=4,200$  V/m,  $S_{in}=0.7$ ).

case of lower frequency. This is because higher frequency (which corresponds to a higher energy absorbed, as in Eq. (1)) can cause moisture to transport upward at a higher rate than that in the case of lower frequency. However, the ease with which the water can move in the liquid phase depends on the nature of the matrix structure within the porous material. In fact, for capillary porous materials, a natural redistribution of the moisture occurs from inside the material as water evaporates at the surface.

As shown in Fig. 8, total pressure distributions up to 5 h are partly a vacuum because the gases formed do not fill in the voids completely. Five hours later, total pressure rapidly builds up within the sample. The amount of accumulated vapor due to the high diffusive vapor flux contributes to a fast increase in total pressure. Overall, the pressure keeps rising with time. High temperature and pressure gradient are generated within the sample, particularly during the constant rate period, initiating a

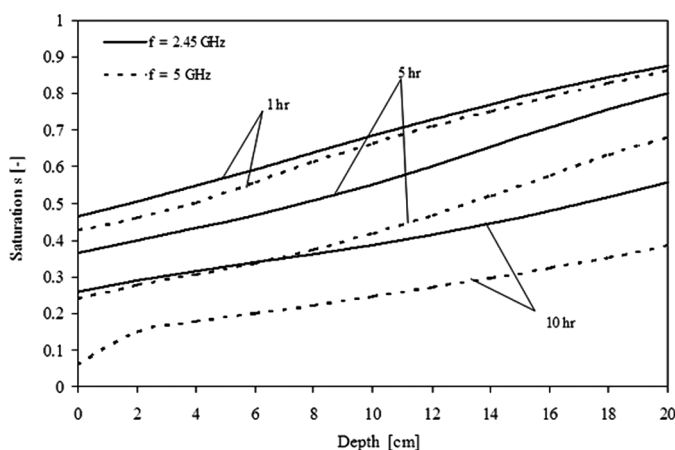


FIG. 7. Moisture profiles at various frequencies ( $d=0.15$  mm,  $E_{in}=4,200$  V/m,  $S_{in}=0.7$ ).

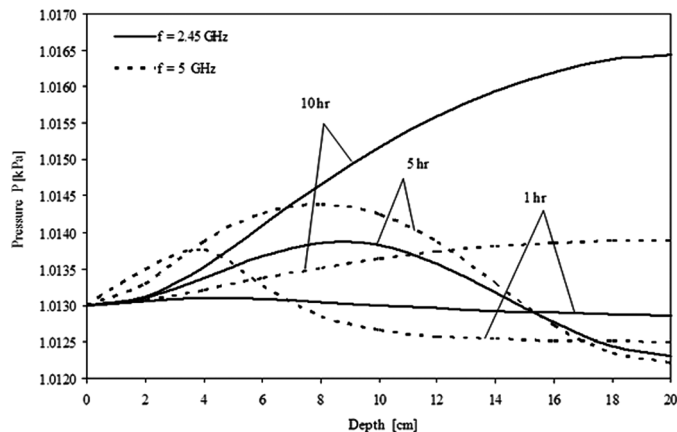


FIG. 8. Pressure distribution at various frequencies ( $d=0.15$  mm,  $E_{in}=4,200$  V/m,  $S_{in}=0.7$ ).

pumping effect. As a result, a great amount of liquid is supplied to the surface. The mechanism of moisture transfer is mainly influenced by capillary pressure.

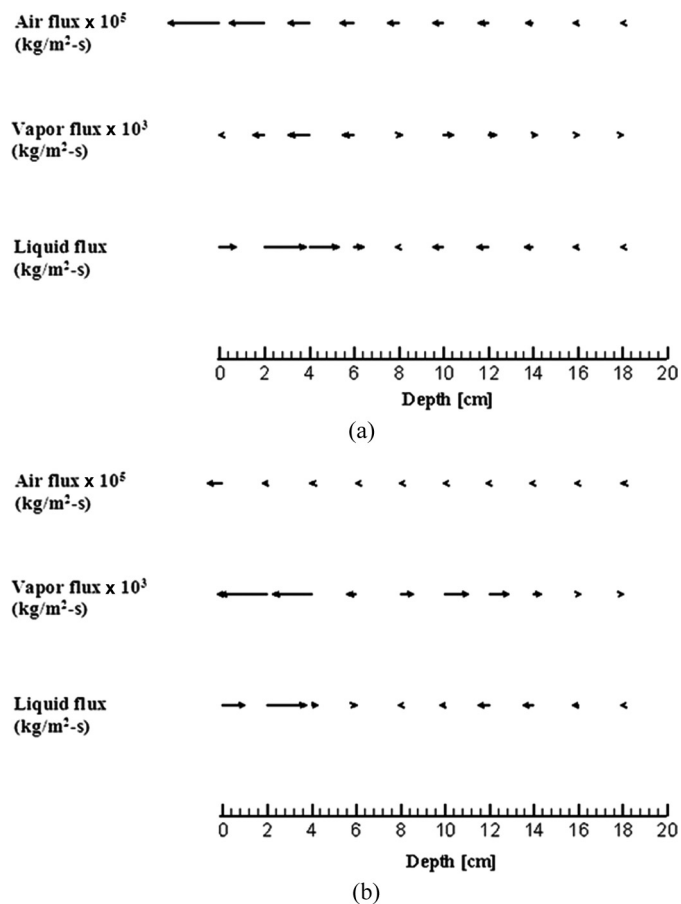


FIG. 9. Fluid movement pattern at 4 h in case of frequency (a) 2.45 GHz (vector length [relative]: 30 grid units/magnitude) and (b) 5 GHz (vector length [relative]: 10 grid units/magnitude).

In order to get more insight into the fluid transport, it is important to study the fluid movements within the sample in depth. The profiles of liquid flux, vapor flux, and air flux for the cases of frequency  $f=2.45$  GHz and  $f=5$  GHz at various times are shown in Figs. 9 and 10, respectively. The results show the same trends for both cases. It can be seen in Fig. 9a that most of the vapor flows within the sample to the surface where evaporation takes place. During the 4th hour, vapor and liquid flow in both directions but opposite to each other because liquid vaporizes, whereas vapor condenses, along the path. Air moves toward the heated surface at the smallest rate. Vapor flux is greater than air flux because convective vapor flux enhances vapor diffusion, whereas convective air flow slows down air diffusion. In the 10th hour (Fig. 10), vapor throughout the medium migrates in the direction of decreasing saturation. As the rate of liquid supply to the surface becomes lower than the evaporation rate, the void volume increases, allowing air to flow away from the heated surface toward the other surface. Figures 11a and 11b depict the evolution of the flux profiles at a depth of

4 cm in the cases of two different frequencies, 2.45 and 5 GHz. The observed vapor flux moves from inside to the surface at the 4th and 2nd hours in cases of microwave frequency at 2.45 and 5 GHz, respectively. However, the quantity of vapor flux at 5 GHz is higher than that found in the case of 2.45 GHz. The higher frequency (which corresponds to a higher energy absorbed, as shown in Fig. 5) can cause moisture to transport upwards at a higher rate than that in the case of lower frequency.

### Influence of Particle Size

Particle size is directly related to water saturation in the packed bed. Water saturation is defined as the fraction of the ratio of water volume to pore volume that means the large particle size have low water saturation. That is, the space among the large particles is smaller than the space

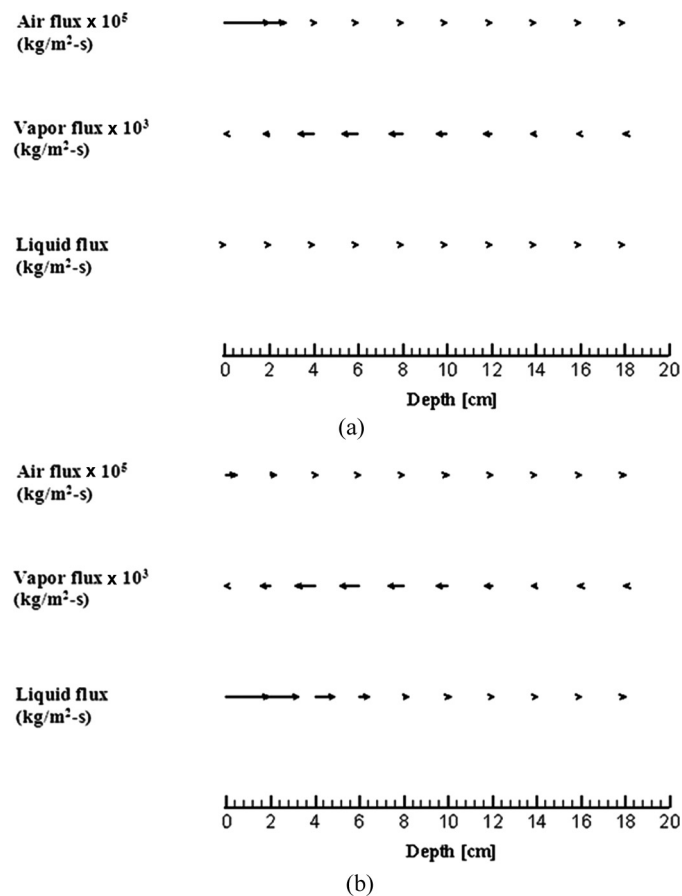


FIG. 10. Fluid movement pattern at 10h in case of frequency (a) 2.45 GHz (vector length [relative]: 1 grid units/magnitude) and (b) 5 GHz (vector length [relative]: 12 grid units/magnitude).

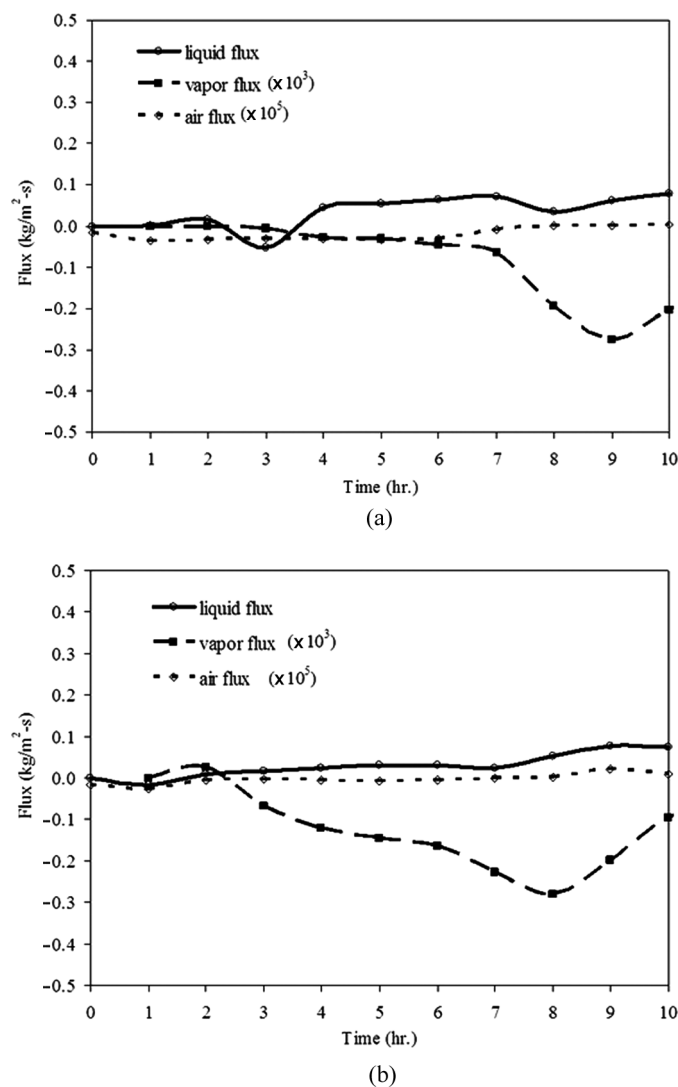


FIG. 11. Flux profiles at 4 cm in case of frequency (a) 2.45 GHz and (b) 5 GHz ( $d=0.15$  mm,  $E_{in}=4,200$  V/m,  $S_{in}=0.7$ ).

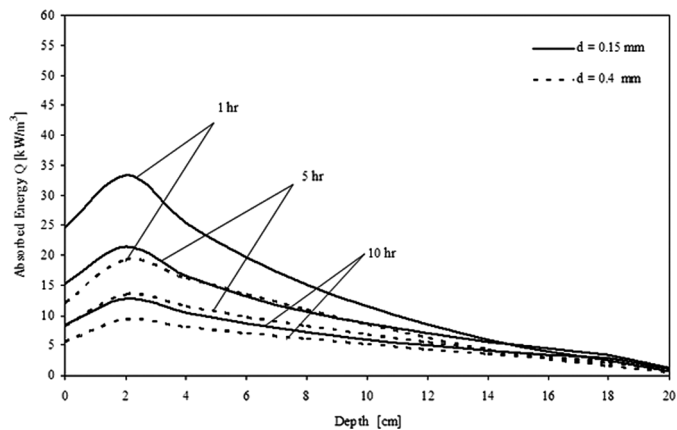


FIG. 12. Energy-absorbed profiles at various particle sizes ( $f = 2.45$  GHz,  $E_{in} = 4,200$  V/m,  $S_{in} = 0.7$ ).

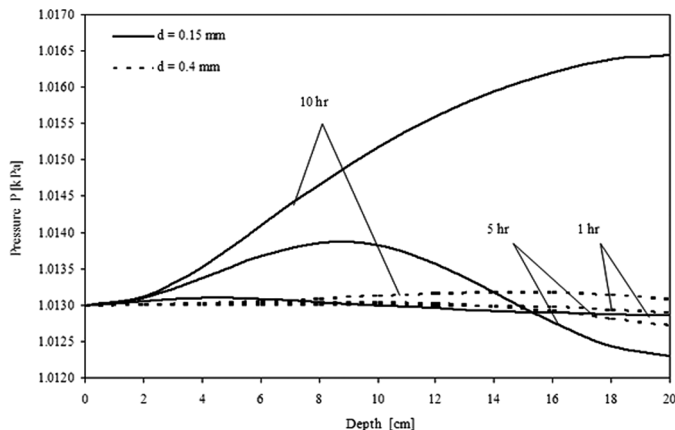


FIG. 15. Pressure distribution at various particle sizes ( $f = 2.45$  GHz,  $E_{in} = 4,200$  V/m,  $S_{in} = 0.7$ ).

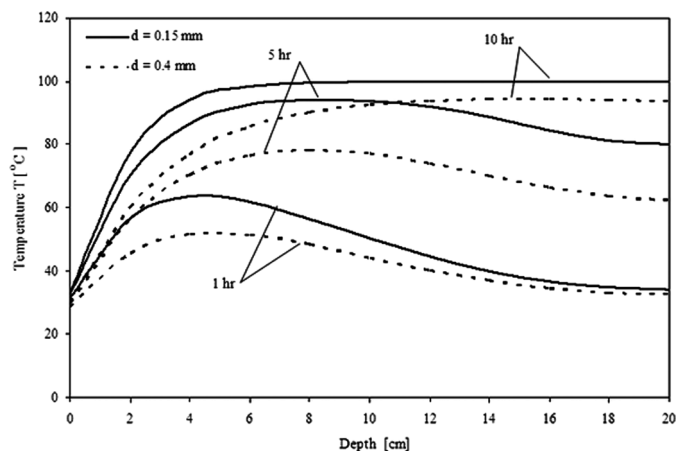


FIG. 13. Temperature profiles at various particle sizes ( $f = 2.45$  GHz,  $E_{in} = 4,200$  V/m,  $S_{in} = 0.7$ ).

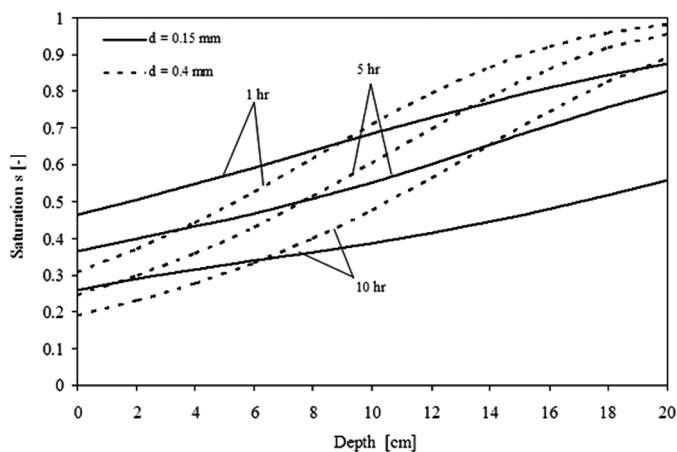


FIG. 14. Moisture profiles at various particle sizes ( $f = 2.45$  GHz,  $E_{in} = 4,200$  V/m,  $S_{in} = 0.7$ ).

between small particles. Therefore, the water content inside a packed bed containing large particles is lower than that in a packed bed containing small particles. The following

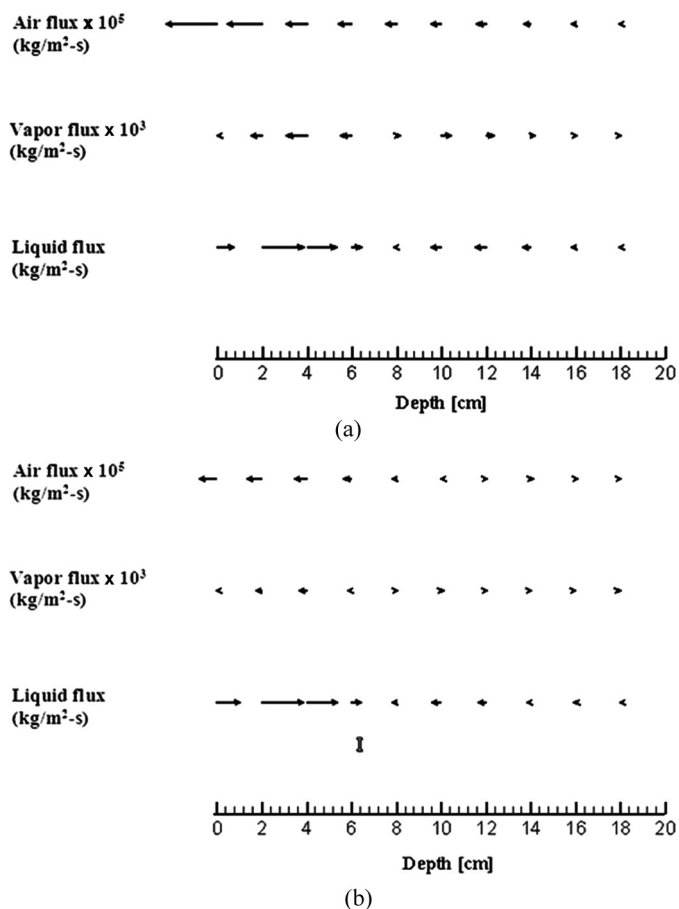


FIG. 16. Fluid movement pattern at 4h in case of particle size (a) 0.15 mm (vector length [relative]: 30 grid units/magnitude) and (b) 0.4mm (vector length [relative]: 65 grid units/magnitude).

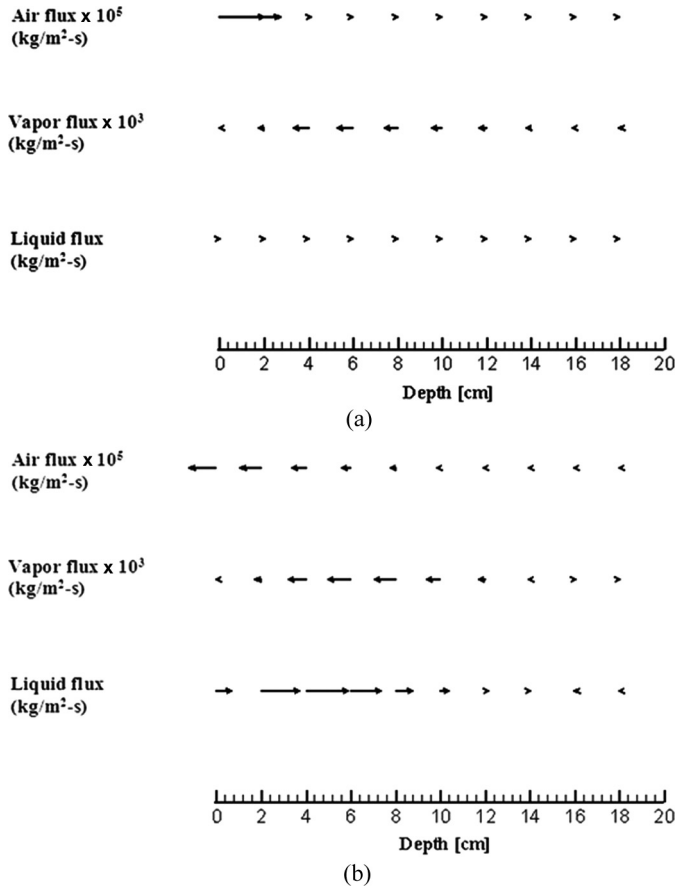


FIG. 17. Fluid movement pattern at 10h in case of particle size (a) 0.15 mm (vector length [relative]: 1 grid units/magnitude) and (b) 0.4 mm (vector length [relative]: 35 grid units/magnitude).

discussion refers to the effect of glass bead size under the same conditions. The microwave energy absorbed, temperature profiles, moisture profiles, and pressure distribution are shown in Figs. 12–15, respectively. Figure 14 shows the moisture profiles for two particle sizes ( $d=0.15$  mm and  $d=0.4$  mm), based on a frequency of 2.45 GHz, electric field intensity of 4,200 V/m, and initial moisture content of 0.7. The observed moisture profiles near the heated edge of the sample in the case of small particle size are higher than the others because a higher capillary force causes moisture to reach the surface at a higher rate than in the case of large particle size due to the microwave energy absorbed (Fig. 12). Figure 13 shows the temperature profiles at various particle sizes. It is found that the temperature of the small particle is higher than the large particle at all drying times, because the moisture content for the small particle is higher and hence more microwave energy is absorbed. Figure 15 shows that total pressure is much higher when a long drying time is reached. Figures 16 and 17 depict the fluid movement patterns within the sample as a function of depth during the 4th

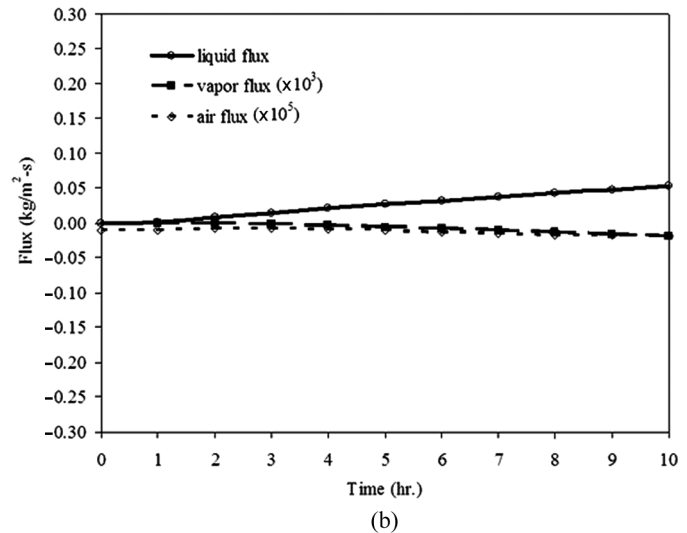
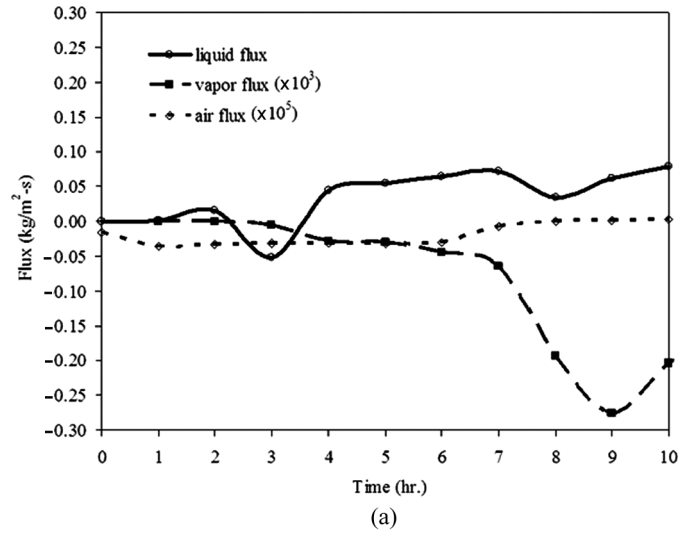


FIG. 18. Flux profiles at 4 cm in case of particle size (a) 0.15 mm and (b) 0.4 mm ( $f=2.45$  GHz,  $E_{in}=4,200$  V/m,  $S_{in}=0.7$ ).

and 10th hours, respectively. The vector profile presented has an advantage of better clarification over the directions and magnitudes. In Figs. 16a and 16b, during the 4th hour, the vapor and liquid flow in both directions with different orders of magnitude, because liquid vaporizes, whereas vapor condenses, along its path. In addition, the result of the small particle size has a larger flux than the larger particle size. (The ratios of grid units to magnitude in the case of small particle size and larger particle size are 30 and 65, respectively.) However, the air flux of 0.15 mm particle size moves toward the surface, but in the case of 0.4 mm size the air flows in the opposite direction because of the effect of capillary pressure. Figure 17a describes the flux profile of 0.15 mm size during the 10th hour. It was found that the vapor flows throughout, and has a higher rate near the central region into which it migrates, in the

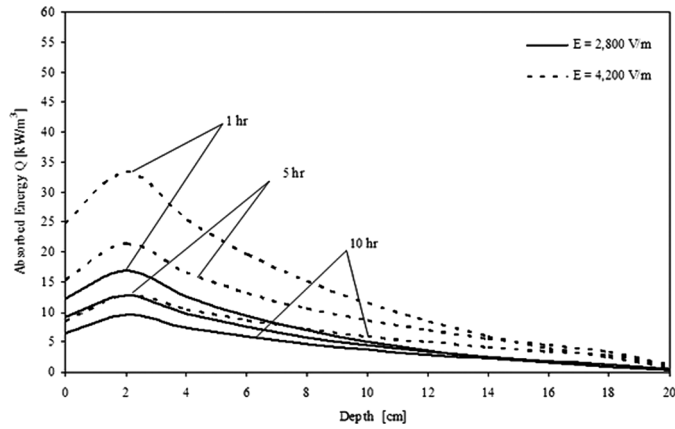


FIG. 19. Energy-absorbed profiles at various electric field intensities ( $f=2.45$  GHz,  $d=0.15$  mm,  $S_{in}=0.7$ ).

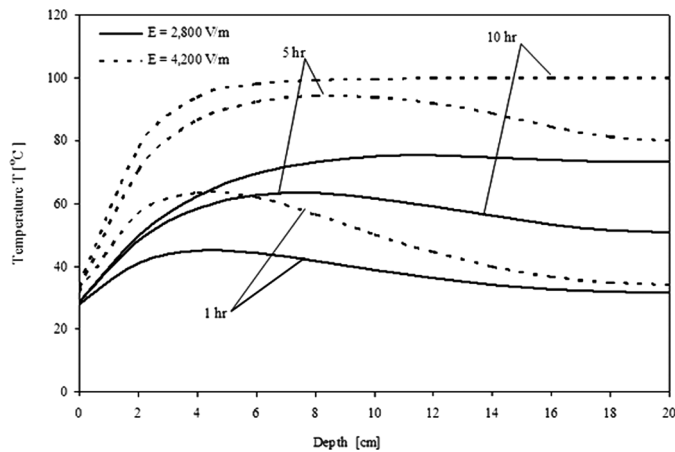


FIG. 20. Temperature profiles at various electric field intensities ( $f=2.45$  GHz,  $d=0.15$  mm,  $S_{in}=0.7$ ).

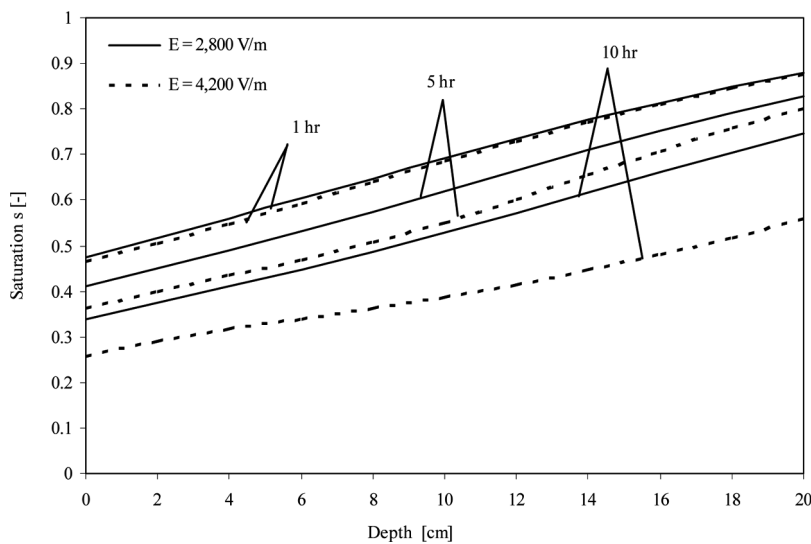


FIG. 21. Moisture profiles at various electric field intensities ( $f=2.45$  GHz,  $d=0.15$  mm,  $S_{in}=0.7$ ).

direction of decreasing saturation. In the case of 0.4 mm (Fig. 17b), the vapor and liquid flow in the opposite directions, as observed previously. The larger particle size (which corresponds to a higher moisture profile, as shown in Fig. 14) causes moisture to transport upward at a lower rate than in the case of small particle size. The flux profiles for two different particle sizes ( $d=0.15$  mm and  $d=0.4$  mm) as a function of time at a depth of 4 cm are shown in Figs. 18a and 18b, respectively. The flux profiles in the case of small particle size exhibit larger magnitudes than those in the case of larger particle size because small particle size corresponds to a higher capillary force and causes moisture to transport upward at a higher rate than in the case of large particle size.

### Influence of Electric Field Intensity

The following discussion focuses on the effect of electric field intensity under the following conditions: frequency of 2.45 GHz, particle size of 0.15 mm, and initial moisture content of 0.7. The microwave energy absorbed for two different electric field intensities ( $E_{in}=2,800$  V/m and  $E_{in}=4,200$  V/m) as a function of distance at various times is shown in Fig. 19. The microwave energy absorbed whose maximum value occurs inside the medium decreases with time. Therefore, continued drying would eventually cause the average moisture content inside the sample to decrease and consequently lead to decreased microwave energy absorbed. The observed microwave energy in the case of higher electric field intensity is higher than that in the case of lower electric field intensity because the energy absorbed is proportional to an electric field intensity as indicated in Eq. (1).

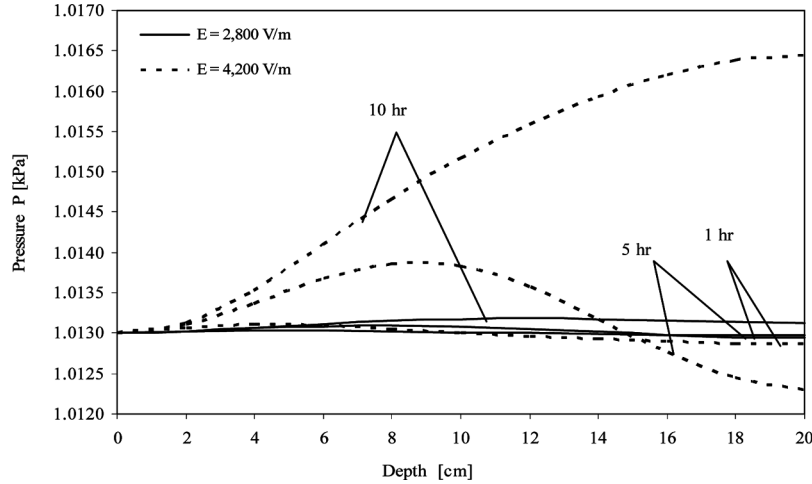
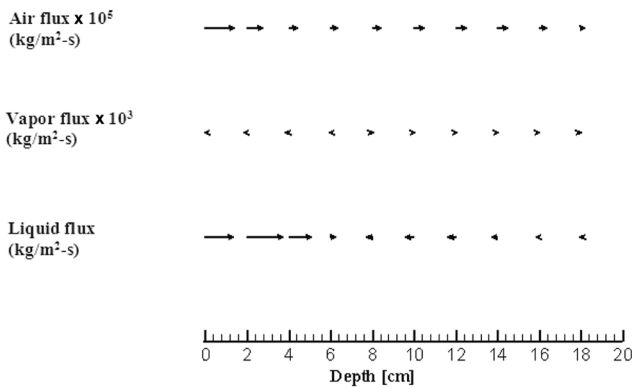


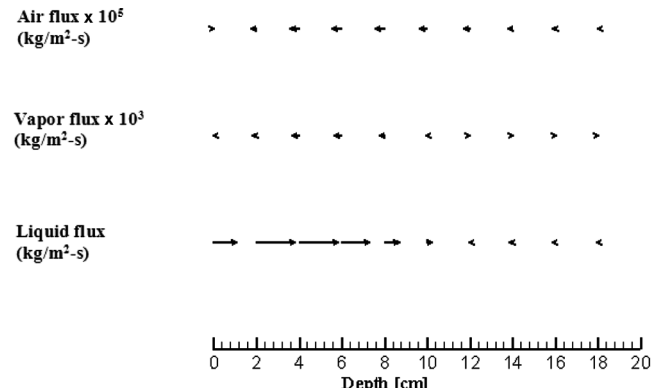
FIG. 22. Pressure distribution at various electric field intensities ( $f=2.45$  GHz,  $d=0.15$  mm,  $S_{in}=0.7$ ).

Accordingly, temperature profiles within the sample in the case of higher electric field intensity are higher than those in the case of lower electric field intensity, as shown in Fig. 20. In Fig. 21, it is observed that the electric field

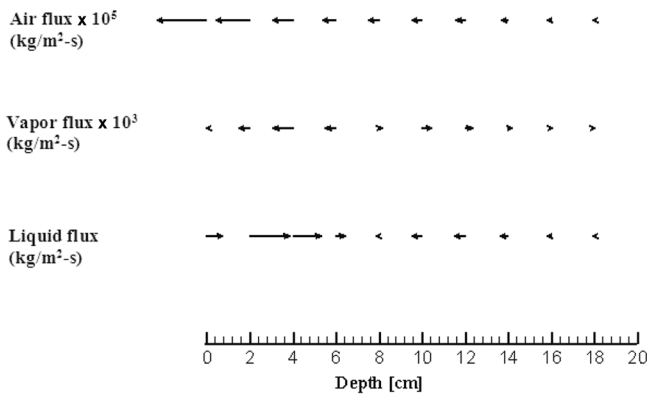
intensity peaks near the high-temperature side, where moisture is relatively low. Figure 22 shows the distributions of pressure within the medium. During the 10th hour, pressure in the case of higher electric field intensity is much



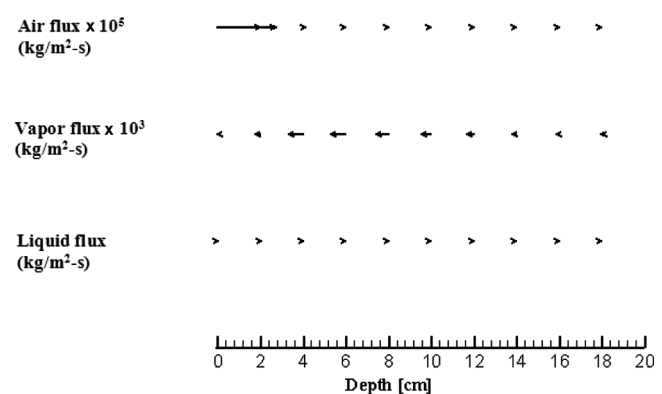
(a)



(a)



(b)



(b)

FIG. 23. Fluid movement pattern at 4 h in case of electric field intensity (a) 2,800 V/m (vector length [relative]: 150 grid units/magnitude) and (b) 4,200 V/m (vector length [relative]: 30 grid units/magnitude).

FIG. 24. Fluid movement pattern at 10 h in case of electric field intensity (a) 2,800 V/m (vector length [relative]: 100 grid units/magnitude) and (b) 4,200 V/m (vector length [relative]: 1 grid unit/magnitude).

higher than that of lower intensity due to much higher temperature in the high-intensity case, as previously seen in Fig. 20. For high intensity, there a vacuum appears during the 5th hour. This vacuum is attributed to an increase in void volumes where vapor and air are formed. The fluid movement patterns within the sample during the 4th and 10th hours are shown in Figs. 23 and 24, respectively. Figures 25a and 25b depict flux profiles during the 4th hour in the cases of electric field intensity of 2,800 V/m and 4,200 V/m, respectively. For both cases, the directions of movement of vapor and liquid fluxes are opposite. Liquid is converted into vapor as vapor concurrently condenses. The magnitudes of flux in the case of electric field intensity of 4,200 V/m are greater than that in case of 2,800 V/m (grid units per magnitude are 30 and 150, respectively). Additionally, at 4,200 V/m, the propagation of air flux is toward the surface, whereas at 2,800 V/m, the air flows in the opposite direction, due to the effect of capillary pressure. Figure 24a shows the electric field intensity of 2,800 V/m during the 10th hour. It was confirmed that

the vapor and liquid flow in opposite directions. Figure 24b shows the case of electric field intensity 4,200 V/m. Liquid and air flux move in the same direction as the air fills up spaces from which the liquid flows. Figures 25a and 25b show the flux profiles within the sample (4 cm) as a function of time. Although transient flow patterns exist in the early stage of drying for 4,200 V/m in Fig. 25b, it has been observed that vapor flux moves from inside to the surface, whereas liquid moves in the opposite direction. The higher electric field intensity gives larger flux magnitudes than for lower electric field intensity because the energy absorbed is proportional to an electric field intensity, as indicated in Eq. (1) (consistent with a higher energy absorbed, as shown in Fig. 19).

## CONCLUSIONS

The numerical model presented in this work describes many of the important interactions within a capillary porous material during microwave drying. The effects of various parameters on the microwave drying process are investigated. Effects of controlled parameters including frequency, particle size, and electric field intensity on heat and mass transport are summarized as follows:

1. A generalized mathematical model of drying by microwave energy is proposed. It is used successfully to describe the drying phenomena under various conditions.
2. The effects of irradiation time, frequency, particle size, and electric field intensity on the microwave drying kinetics are clarified in detail, taking into account the influence of vapor diffusion and capillary flow.
3. Moisture transports near the heated edge of the sample in the case of higher frequency are higher than those in the case of lower frequency. This is because the higher frequency, which corresponds to a higher energy absorbed, causes moisture to reach the surface at a higher rate.
4. Pressure built up near the heated surface is attributed to high diffusive flux of accumulated vapor inside the medium.
5. The small bead size leads to much higher capillary forces, resulting in a faster drying time.
6. The fluid movements in porous media depend on the size of the pores, the size of the particles, and the fluid flow rate.

Additionally, in this work, the microwave energy absorbed was assumed to decay exponentially into the sample, according to Lambert's law. This assumption is valid for the large dimensions of the sample as considered in the study. For a small sample, the spatial variations of the electromagnetic field and microwave energy absorbed within the sample must be obtained by a complete solution of the unsteady Maxwell's equations. Finally, the findings

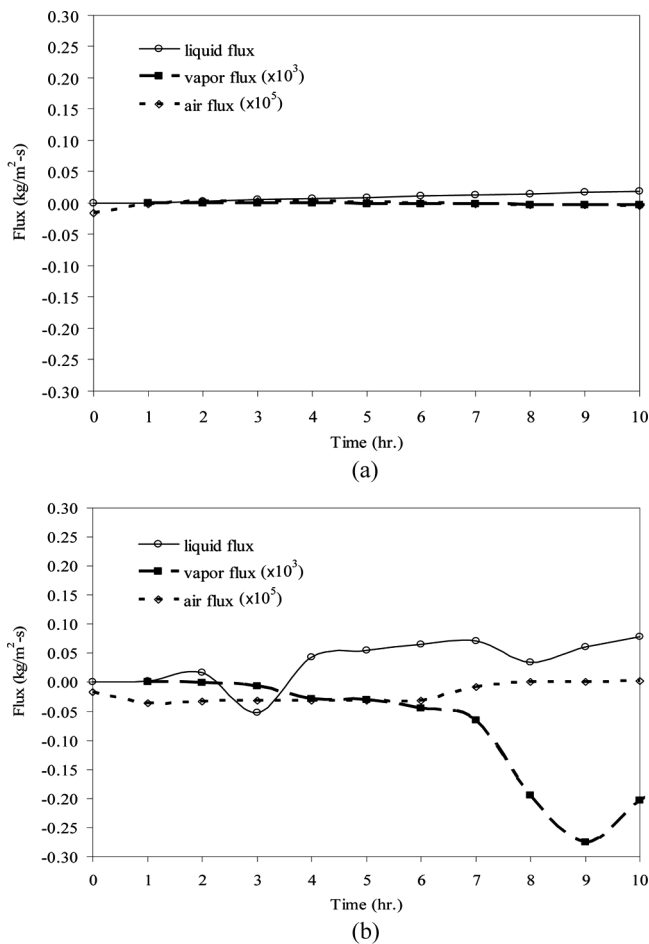


FIG. 25. Flux profiles at 4 cm in case of electric field intensity (a) 2,800 V/m and (b) 4,200 V/m ( $f = 2.45$  GHz,  $d = 0.15$  mm,  $S_m = 0.7$ ).

of this study are significant and can lead to further research, conducted along similar lines, as well as to applications related to the heat and mass transfers in porous media.

## NOMENCLATURE

$c$	Velocity of light (m/s)
$D_m$	Effective molecular mass diffusion ( $\text{m}^2/\text{s}$ )
$D_p$	Penetration depth (m)
$E$	Electric field intensity (V/cm)
$f$	Frequency (GHz)
$g$	Gravitational constant ( $\text{m}/\text{s}^2$ )
$H_v$	Specific heat of vaporization (J/kg)
$h_c$	Heat transfer constant ( $\text{W}/\text{m}^2\text{K}$ )
$h_m$	Mass transfer constant ( $\text{W}/\text{m}^2\text{K}$ )
$k$	Permeability ( $\text{m}^2$ )
$\dot{n}$	Phase change term ( $\text{kg}/\text{m}^3\text{s}$ )
$P$	Microwave power (W)
$p$	Pressure (Pa)
$Q$	Microwave power absorbed term ( $\text{W}/\text{m}^3$ )
$S$	Water saturation
$T$	Temperature ( $^\circ\text{C}$ )
$t$	Time (s)
$w$	Velocity (m/s)

## Greek Letters

$\tan \delta$	Loss tangent coefficient
$\delta_s$	Skin depth
$\varepsilon$	Complex permittivity (F/m)
$\varepsilon'$	Permittivity or dielectric constant
$\varepsilon''$	Dielectric loss factor
$\lambda$	Effective thermal conductivity ( $\text{W}/\text{mK}$ )
$\mu$	Magnetic permeability (H/m)
$\mu_g$	Dynamic viscosity of gas (Pa s)
$\mu_l$	Dynamic viscosity of liquid (Pa s)
$\rho$	Density ( $\text{kg}/\text{m}^3$ )
$\phi$	Porosity

## Subscripts

0	Free space
A	Air
c	Capillary
g	Gas
l	Liquid water
p	Particle
r	Relative
v	Water vapor
x	Coordinate axis

## ACKNOWLEDGMENT

The authors thank the Commission on Higher Education, Thailand, for supporting by grant fund under the program Strategic Scholarships for Frontier Research

Network for the Joint Ph.D. Program Thai Doctoral degree for this research.

## REFERENCES

- Clemens, J.; Saltiel, C. Numerical modeling of materials processing in microwave furnaces. *International Journal of Heat and Mass Transfer* **1996**, *39* (8), 1665–1675.
- Hill, J.M.; Marchant, T.R. Modelling microwave heating. *Applied Mathematical Modelling* **1996**, *20* (1), 3–15.
- Turner, I.W.; Puiggali, J.R.; Jomaa, W. A numerical investigation of combined microwave and convective drying of a hygroscopic porous material: A study based on pine wood. *Transactions of the Institution of Chemical Engineers* **1998**, *76*, 193–209.
- Bows, J.R.; Patrick, M.L.; Janes, R.; Metaxas, A.C. Microwave phase control heating. *International Journal of Food Science and Technology* **1999**, *34*, 295–304.
- Ni, H.; Datta, A.K.; Torrance, K.E. Moisture transport in intensive microwave heating of biomaterials: A multiphase porous media model. *International Journal of Heat and Mass Transfer* **1999**, *42*, 1501–1512.
- Boukadida, N.; Ben Nasrallah, S.; Perre, P. Mechanism of heat and mass transfer during convective drying of porous media under different drying conditions. *Drying Technology* **2000**, *18*, 1367–1388.
- Wang, Z.H.; Chen, G. Heat and mass transfer in batch fluidized-bed drying of porous particles. *Chemical Engineering Science* **2000**, *55*, 1857–1869.
- Zhao, H.; Turner, I.W. The use of a coupled computational model for studying the microwave heating of wood. *Applied Mathematical Modelling* **2000**, *24* (3), 183–197.
- Feng, H.; Tang, J.; Cavalieri, R.P.; Plumb, O.A. Heat and mass transport in microwave drying of porous materials in a spouted bed. *AIChE Journal* **2001**, *47*, 1499–1512.
- Ratanadecho, P.; Aoki, K.; Akahori, M. Experimental and numerical study of microwave drying in unsaturated porous material. *International Communications in Heat and Mass Transfer* **2001**, *28*, 605–616.
- Ratanadecho, P.; Aoki, K.; Akahori, M. Influence of irradiation time, particle sizes and initial moisture content during microwave drying of multi-layered capillary porous materials. *ASME Journal of Heat Transfer* **2002**, *124* (1), 151–161.
- Ratanadecho, P. The simulation of microwave heating of wood using a rectangular wave guide: Influence of frequency and sample size. *Chemical Engineering Science* **2006**, *61*, 4798–4811.
- Perré, P. Multiscale aspects of heat and mass transfer during drying. *Transport in Porous Media* **2007**, *66*, 59–76.
- Rattanadecho, P.; Pakdee, W.; Stakulcharoen, J. Analysis of multi-phase flow and heat transfer: Pressure buildup in an unsaturated porous slab exposed to hot gas. *Drying Technology* **2008**, *26*, 39–53.
- Niamnuy, C.; Devahastin, S.; Soponronnarit, S.; Vijaya Raghavan, G.S. Modeling coupled transport phenomena and mechanical deformation of shrimp during drying in a jet spouted bed dryer. *Chemical Engineering Science* **2008**, *63* (22), 5503–5512.
- Chemkhi, S.; Jomaa, W.; Zagrouba, F. Application of a coupled thermo-hydro-mechanical model to simulate the drying of non-saturated porous media. *Drying Technology* **2009**, *27*, 842–850.
- Villa-Corrales, L.; Flores-Prieto, J.J.; Xamán-Villaseñor, J.P.; García-Hernández, E. Numerical and experimental analysis of heat and moisture transfer during drying of Ataulfo mango. *Journal of Food Engineering* **2010**, *98* (2), 198–206.
- Mujumdar, A.S. *Handbook of Industrial Drying*, 2nd ed.; Marcel Dekker: New York, 1995.
- Metaxas, A.C.; Meredith, R.J. *Industrial Microwave Heating*; Peter Peregrinus Ltd.: London, 1983.

20. Datta, A.K.; Anantheswaran, R.C. *Handbook of Microwave Technology for Food Applications*; Marcel Dekker: New York, 2001.
21. Schubert, H.; Regier, M. *The Microwave Processing of Foods*; Woodhead Publishing Limited: Cambridge, UK, 2005.
22. Perré, P.; May, B.K. A numerical drying model that accounts for the coupling between transfers and solid mechanics: Case of highly deformable products. *Drying Technology* **2001**, *19* (8), 1629–1643.
23. Wang, J.; Schmugge, T. An empirical model for the complex dielectric permittivity of soil as function of water content. *IEEE Transactions on Geoscience and Remote Sensing* **1980**, *18* (4), 288–295.
24. Von Hippel, A.R. *Dielectric Materials and Applications*; MIT Press: Boston, 1954.
25. Patankar, S.V. *Numerical Heat Transfer and Fluid Flow*; McGraw-Hill: New York, 1980.
26. Kaviany, M.; Rogers, J. Funicular and evaporative-front regimes in convective drying of granular beds. *International Journal of Heat and Mass Transfer* **1992**, *35* (2), 469–480.